Microchemical Journal 214 (2025) 113954

Contents lists available at ScienceDirect

Microchemical Journal

journal homepage: www.elsevier.com/locate/microc

A Y-shape-structured photoelectrochemical biosensor based on Bi_4NbO_8Cl/TiO_2 heterojunction and enzyme-mediated electrocatalysis for sensitive and selective determination of microRNA in serum

Yu Zhong, Zhi-Wei Xu, Zhang-Jian Cheng, Ai-Lin Liu *, Yun Lei *

Department of Pharmaceutical Analysis, The School of Pharmacy, Fujian Medical University, Fuzhou 350122, China

ARTICLE INFO

Keywords:
Photoelectrochemical biosensor
Perovskite
Heterojunction
Y-shaped junction structure
Electron donor
MicroRNA

ABSTRACT

Accurate and sensitive detection of microRNAs (miRNAs) in tumorigenesis has posed a great challenge, as its characteristics of ultra-low abundance and high sequence homology. In this approach, a highly sensitive and selective Y-shape-structured photoelectrochemical (PEC) biosensor coupled with dual signal amplification strategy was constructed with introduction of heterojunction nanocomposite and *in situ* enzymatic generation of electron donor. Specifically, Bi_4NbO_8Cl/TiO_2 heterojunction allowed for efficient electron transport, further achieved the electrons-holes pairs separation, and thus greatly improved photocurrent intensity. Alkaline phosphatase (ALP) modified with auxiliary probes catalyzes hydrolysis of ascorbic acid 2-phosphate (AAP) to *in situ* generate ascorbic acid (AA) as electron donors for further signal amplification. Furthermore, hairpin capture probes with rigid structure were immobilized upright on electrode surface and stable Y-shaped junction configurations were formed away from the electrode surface, which was beneficial to avoid probes' self-entanglement, improve the hybridization efficiency and enhance the recognition ability. As a proof-of-concept, the Y-shape-structured PEC biosensor coupled with dual signal amplification tactic achieves accurate quantification of miRNA-222 (papillary thyroid carcinoma-relevant biomarker) with salient selectivity, rapid response and low detection limit (0.15 pM, S/N = 3). The proposed PEC biosensor displays potential applications in tumor-related miRNAs assay for tumor prediction, diagnosis and prognosis.

1. Introduction

MicroRNAs (miRNAs), a class of endogenous non-coding RNAs with a size of 18 – 24 nucleotides, have capacity to regulate numerous malignant tumor-relevant processes through degrading or inhibiting the translation of target gene [1,2]. Dysregulated expression of miRNAs has been verified in various tumors, suggesting their potential as diagnostic and prognostic biomarkers [3,4]. Consequently, the development of accurate and rapid miRNA assays has become a vital issue for clinical diagnosis, gene therapy and cancer prognosis research. Current methodologies used for miRNA detection include fluorescence, capillary electrophoresis, surface-enhanced Raman spectroscopy, electrochemistry, electrochemiluminescence (ECL), photoelectrochemistry and so on [5–7]. Among these, with virtues of low limit-of-detection, improved signal-to-noise ratio, cost-effective apparatus and undemanding experimental conditions, photoelectrochemical (PEC) bioanalysis has been applied in the detection of cancer-associated miRNAs [8–12].

As the core element, photoactive materials play a crucial role in sensitivity enhancement of PEC biosensors. Perovskite materials possess high charge-carrier mobility, unique carrier separation property, adjustable band gap and high light absorption coefficient [13,14]. Particularly, Bi_4NbO_8Cl, a single-layer Sillen-Aurivillius perovskite phase introduced by J. F. Ackerman, is composed of single layer NbO_4 perovskite blocks isolated by $(Bi_2O_2)_2Cl$ blocks [15]. Importantly, the hybridization of Bi 6 s with O 2p orbitals in Bi_4NbO_8Cl compound is beneficial to fast carrier mobility, and Bi_4NbO_8Cl is also distinguished for its merits of water-tolerant ability, photocatalytic activity and narrow band gap [16]. For PEC biosensors, the efficacy of optical-to-electrical signal transduction is related to the efficient separation of photogenerated carriers. However, the inherent high charge-carrier recombination rate and low photocurrent response limit the utility of mere perovskite in meeting the needs of PEC biosensing applications. Adopting perovskite heterostructures at the nanoscale, where perovskites are coupled with one or more materials within a single building

* Corresponding authors.
E-mail addresses: ailinliu@fjmu.edu.cn (A.-L. Liu), leiyun@fjmu.edu.cn (Y. Lei).

https://doi.org/10.1016/j.microc.2025.113954
Received 10 February 2025; Received in revised form 20 April 2025; Accepted 12 May 2025
Available online 13 May 2025

block, has been considered as a prevailing approach to transport the photo-induced charge carriers from one to another counterpart (with electrons and holes typically migrating in opposite directions across the interface), thus suppressing recombination, increasing photo-excited carrier lifetimes and enhancing photocurrent signal [17–19]. For instance, Ruan *et al.* reported a PEC sensor based on gold nanoparticles (AuNPs) equipped with perovskite Bi_4NbO_8Cl heterostructure through layer-by-layer self-assembly, showing greatly incremental photocurrent signal compared with a bare perovskite electrode [20]. The common heterostructured materials involve metal oxides, chalcogenide semiconductors, noble metals and various combinations thereof.

Titanium dioxide (TiO_2), as a member of metal oxide family, has merits of excellent biocompatibility, large specific surface area, high resistance to photocorrosion and steady chemical property, so it occupies an important position in PEC biosensor applications [21,22]. For spatial modulation of electrons and holes, the synergic effect between perovskite Bi_4NbO_8Cl and TiO_2, leveraging their complementary band gap, is an ideal scheme. Gao *et al.* [23] reported a paper-based PEC biosensor with TiO_2/Bi_4NbO_8Cl/Co-Pi cascade structure, where TiO_2 nanosheet array serves as electron transporting material, cobalt phosphate (Co-Pi) acts as hole transporting material and Bi_4NbO_8Cl works as a light harvester, enabling the bidirectional modulation of charge carrier separation. Regrettably, the Bi_4NbO_8Cl-modified TiO_2 nanosheet array was synthesized through a vacuum vapor phase deposition method, which is subject to complicated operation and high cost. As such, developing a simple and green method bestows immense possibilities on PEC biosensors in a routine laboratory setting.

Currently, PEC biosensors have long been plagued by the limited accessibility of target sequences to the capture probes immobilized on heterogeneous surfaces. With this in mind, the adoption of Y-shaped DNA junction structures can achieve effective control of orientation, distribution and packing density [24]. Thereinto, the stem of capture probe serves as a rigid scaffold to keep it upright, and its loop supplies an enclosed platform for the binding of target and auxiliary probe. Of note, the rigid stem can separate the target and auxiliary probe from electrode surface, providing a solution-phase like circumstance for circumvention of self-entanglement of probe, efficient hybridization and sensitivity enhancement. For instance, Li *et al.* [25] reported a dual-thiol modified hairpin capture probe to form a Y-shaped DNA junction, and the developed electrochemical biosensor showed high molecular rigidity, precise control and an attomolar detection limit. Moreover, the introduction of Y-shaped DNA junction structure also plays an instrumental role in specificity improvement. In the absence of target, two probes cannot hybridize owing to the low melting temperature (T_m), but the hybridization and configuration formation occur upon target presence. This structure possesses salient sequence specificity even under mild conditions because of a relatively short duplex formed between target sequence and probes [26,27]. Its integration with PEC biosensors is envisioned to enhance selectivity. For instance, Liu *et al.* [28] developed a highly selective PEC aptasensor for antigen assay based on Y-shaped DNA, demonstrating a significantly enhanced photocurrent signal even at concentrations 100-fold lower than those of the non-target analytes. Our group previously has also developed an ECL biosensor coupled with Y-shaped DNA junction structures for miRNA-222 assay with single-base resolution [24].

In this work, a Y-shape-structured PEC biosensor coupled with dual signal amplification strategy based on layer-by-layer assembled Bi_4NbO_8Cl/TiO_2 heterojunction structure and electron donor-AA generated by ALP catalysis was developed for miRNA determination (Scheme 1). As a proof-of-concept, miRNA-222, transcriptionally up-regulated in papillary thyroid carcinoma (PTC) compared with unaffected thyroid tissue, was selected as a target miRNA [29]. Specifically, the developed Bi_4NbO_8Cl/TiO_2 hybrid took merits of electron transporting material TiO_2 and light absorber Bi_4NbO_8Cl, demonstrating an enhanced photo-to-electric conversion efficiency. Of note, the perovskite Bi_4NbO_8Cl was prepared through simple one-step alkali fusion method. In addition, the stable Y-shaped junction configuration, consisting of a capture probe (CP), an auxiliary probe (AP) modified with AuNPs labeled alkaline phosphatase (ALP-AuNPs-AP) and a target sequence, was self-assembled. Thereinto, ALP could catalyze the hydrolysis of ascorbic acid 2-phosphate (AAP) to *in situ* generate ascorbic acid (AA), which acts as an electron donor. This process quenched photogenerated holes, hindered recombination of photogenerated electron-hole pairs, and enhanced the photocurrent response. Collectively, this work demonstrates the value of efficient electron-hole pairs separation to the sensitivity of PEC sensor and paves the way for the clinical application in the early disease diagnosis, gene therapy and tumor prognosis study.

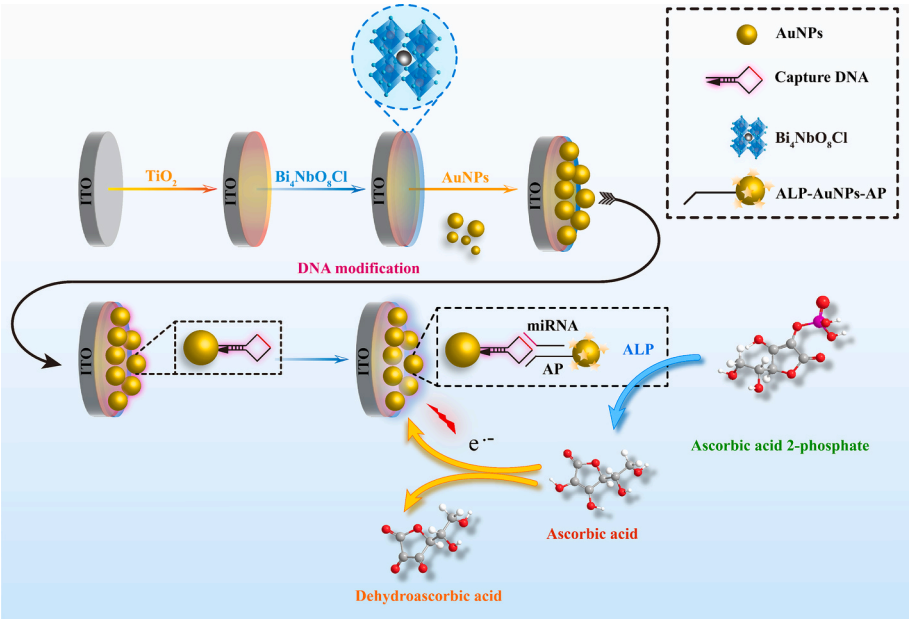

Scheme 1. Schematic illustration of a Y-shape-structured PEC biosensor based on Bi_4NbO_8Cl/TiO_2 heterojunction and enzyme-mediated electrocatalysis for sensitive and selective determination of microRNA.

2. Experimental sections

2.1. Reagents and apparatus

Reagents and apparatus are provided in Supplementary Information.

2.2. Preparation of Bi_4NbO_8Cl

The perovskite Bi_4NbO_8Cl was prepared by simple one-step alkali fusion method. Initially, 0.7277 g CsCl and 0.1360 g NaCl (stoichiometric molar ratio of 1.85:1) were accurately weighed and ground for 20 min in a mortar. A mixture of CsCl and NaCl was used as the molten salt or flux mix. 0.2446 g Bi_2O_3, 0.0912 g BiOCl and 0.0465 g Nb_2O_5 were fully mixed with pre-mixed CsCl/NaCl for about 15 min. Thereinto, Bi_2O_3, BiOCl and Nb_2O_5 were mixed in a stoichiometric molar ratio of 3:2:1. And the Bi_4NbO_8Cl precursors and flux were mixed at a solute concentration of 5 mol% (Bi_4NbO_8Cl/(Bi_4NbO_8Cl + flux)). The mixture was then placed in a corundum crucible and heated to a setting temperature (800 ℃) in muffle furnace for 10 h. After natural cooling, perovskite Bi_4NbO_8Cl was successfully synthesized. Then, Bi_4NbO_8Cl was thoroughly rinsed and dispersed with double distilled water (DDW). The suspension was filtered with a Büchner funnel, and the product was washed with DDW three times, followed by drying at room temperature. Finally, it was redispersed into DDW for further use.

2.3. Preparation of ALP-AuNPs-AP

Auxiliary probes (AP) modified with AuNPs labeled alkaline phosphatase (ALP-AuNPs-AP) conjugates were prepared as follows. Firstly, the pH to the AuNPs solution was adjusted to 8.2 by the dropwise addition of 0.2 M K_2CO_3 under stirring. Secondly, 20 μL of 1 μM AP (sequences displayed in Table S1) and 40 μL of 0.8 mg/mL ALP were successively added into 2 mL AuNPs solution under ice-bath condition for 2 h. Thirdly, 400 μL of 1 mM 6-mercapto-1-hexanol (MCH) was used to block any non-specific active sites for 30 min at room temperature with gentle stirring. Fourthly, the conjugates were ultra-centrifuged at 10,000 rpm for 20 min and then washed with 10 mM phosphate buffered saline (PBS, pH 7.4) three times to remove the residues. The resulting ALP-AuNPs-AP conjugates were dissolved in 200 μL DDW and stored at 4 ℃.

2.4. Fabrication of PEC biosensor

Indium tin oxide (ITO) slices with 2 × 0.8 cm rectangle size were ultrasonically washed by 1 M NaOH, 30 % H_2O_2, acetone and DDW successively for 5 min each to remove surface-adsorbed impurity particles, microorganisms and organic matters. Then the prepared ITO was dried in a vacuum oven for later use. The clean ITO slices were pretreated and served as the working electrodes constructed through a layer-by-layer technique as follows. Firstly, the purchased TiO_2 nanoparticles were calcined in a muffle furnace at 450 ℃ for 2 h. Then, 10 μL of 2 mg/mL TiO_2 solution was applied to a circular working region (6 mm diameter) on the clean ITO electrode, masked with a hole in sellotape. The coated electrode was air-dried at 60 ℃ and calcinated at 450 ℃ in muffle furnace for 2 h. Secondly, 10 μL of 2 mg/mL Bi_4NbO_8Cl suspension was coated on working area of the TiO_2/ITO electrode, dried at 60 ℃ and calcinated at 450 ℃. Thirdly, 10 μL AuNPs solution was added onto the Bi_4NbO_8Cl/TiO_2/ITO electrode and dried under an infrared lamp. Fourthly, 10 μL of 1 μM capture probe (CP) was coated on the surface of AuNPs/Bi_4NbO_8Cl/TiO_2/ITO, then reacted at room temperature for 2 h and washed with tris[hydroxymethyl]aminomethane (Tris)-HCl solution (10 mM, pH 7.4) three times. After vacuum drying, the CP/AuNPs/Bi_4NbO_8Cl/TiO_2/ITO electrode was prepared. Fifthly, 20 μL of 1 mM MCH solution was added on the aforementioned electrode, which was then blocked at room temperature for 1 h, washed with Tris-HCl solution (pH 7.4) three times and vacuum-dried. Sixthly, the hybridization reaction was carried out by dropping a mixture of 10 μL ALP-AuNPs-AP and target miRNA-222 on the electrode at 37 ℃ for 50 min. After that, the resulting sensor was washed with Tris-HCl solution (pH 7.4) three times and vacuum-dried. Finally, the ALP-AuNPs-AP-RNA-CP/AuNPs/Bi_4NbO_8Cl/TiO_2/ITO electrode was placed in 15 mL Tris-HCl solution containing 100 mM AAP at 37 ℃, then was enzymatically hydrolyzed for the later PEC determination.

2.5. Electrochemical and PEC measurement

The electrochemical measurements were performed with an electrochemical system consisted of a modified ITO working electrode, a counter electrode (Pt wire) and an Ag/AgCl reference electrode. PEC measurements were performed by chronoamperometry, a current–time (*i-t*) method, at an applied potential of 0 V. The experimental parameters were set up as follows: 0.001 s sampling interval, 10 s static placing time, 70 s sampling time and 1×10^{-6} sensitivity. The photocatalysts were irradiated with a 300 W xenon lamp equipped with a cutoff filter (CUT 365 nm).

3. Results and discussion

3.1. Detection principle of the PEC biosensor

The detection mechanism of the Y-shape-structured PEC biosensor based on Bi_4NbO_8Cl/TiO_2 heterojunction and enzyme-mediated electrocatalysis for PTC-related miRNA-222 determination was exhibited in Scheme 1. The Bi_4NbO_8Cl/TiO_2 heterojunction as photoactive material was firstly immobilized on ITO surface via a layer-by-layer self-assembly procedure. Secondly, AuNPs modification could enlarge the specific surface area, increase probe loading and enhance the overall conductivity. Thirdly, the sulfhydryl-functionalized hairpin CP was connected to AuNPs via dual Au-S bonds. The stem part of CP, as a rigid structure, kept upright on the electrode surface to avoid the probe entanglement, while the ring part, designed for DNA hybridization, was far away from the electrode surface to facilitate hybridization events. Subsequently, the ALP-AuNPs-AP conjugate was introduced to hybridize with CP and target miRNA-222, and the formed Y-shaped configuration was accessible for the control of orientation, distribution and packing density. Meanwhile, ALP could catalyze the hydrolysis of AAP to *in situ* generate AA as electron donors, which directly quenched the photogenerated holes and suppressed the recombination of photogenerated electron-hole pairs, leading to an evidently enhanced anodic photocurrent. The dual signal amplification tactic leveraging the photocatalytic effect of the Bi_4NbO_8Cl/TiO_2 heterojunction and electron donor, endows the Y-shape-structured biosensor with the capability for sensitive and selective determination of miRNA-222.

3.2. Characterization of materials

The morphology of as-prepared materials was characterized by scanning electron microscope (SEM) and transmission electron microscope (TEM). As shown in the Fig. 1A, Bi_4NbO_8Cl exhibited a relatively rough surface, which was advantageous for further adsorption. The inset of Fig. 1A further demonstrated the well-grown Bi_4NbO_8Cl particles were layered and plate-like shaped at micro-level size. And Bi_4NbO_8Cl presented the lattice with a width of about 0.35 nm (Fig. 1B), corresponding to the (114) lattice plane of Bi_4NbO_8Cl [30]. The TEM images of TiO_2 displayed evenly distribution without obvious agglomeration and the average particle size was approximately 35 nm (Fig. 1C).

Additionally, the crystal structure of the synthesized materials was detected by X-ray diffraction (XRD), as shown in Fig. 1D. The pattern presented a strongest peak (116) at 29.7° that was the characteristic peak of the crystal plane of Bi_4NbO_8Cl synthesized at 800 ℃, meanwhile, the peaks at 23.8°, 32.5°, 46.8° and 56.6° were corresponded to the (112), (200), (220) and (316) planes of Bi_4NbO_8Cl (JCPDS card

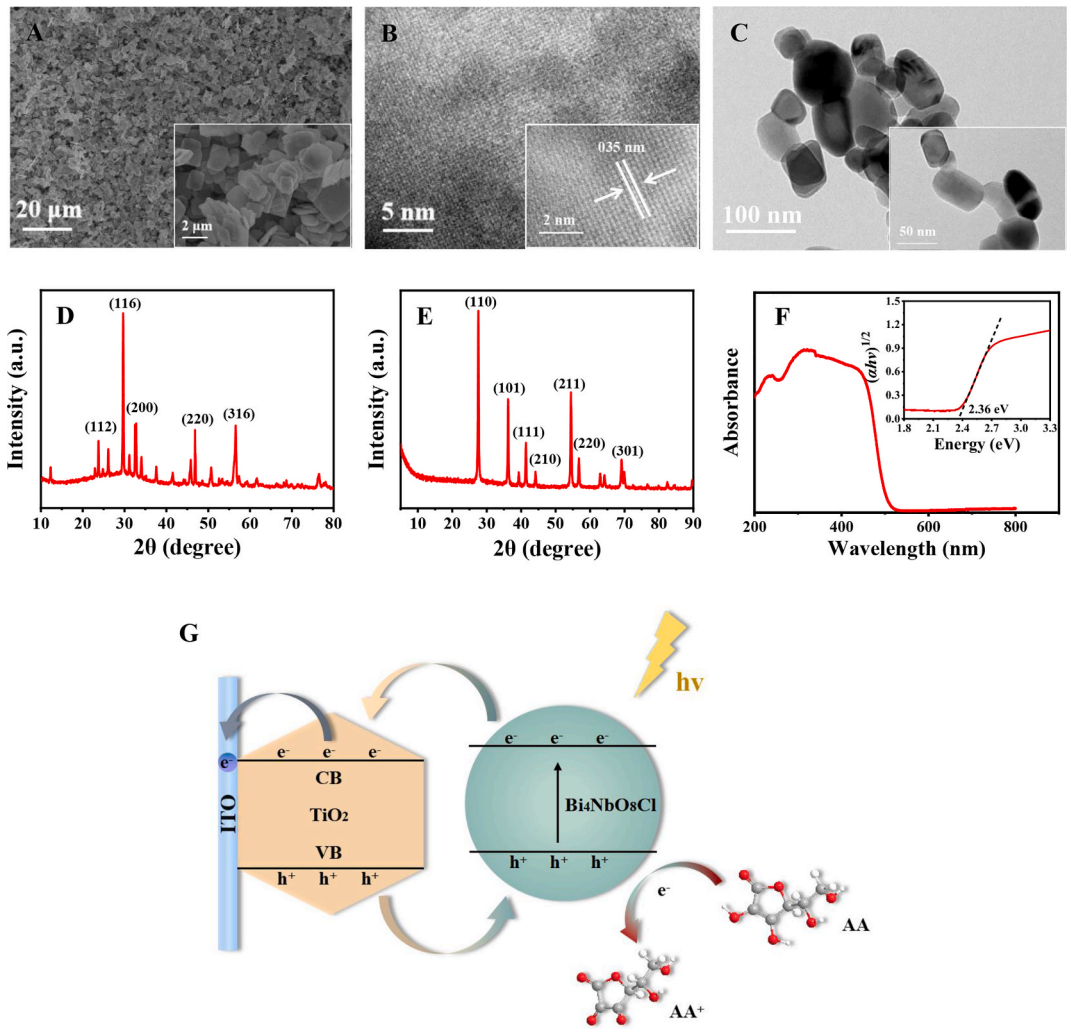

Fig. 1. SEM image (A) and TEM image (B) of Bi_4NbO_8Cl. Insets: High magnification images of Bi_4NbO_8Cl. (C) TEM image of TiO_2. Inset: High magnification image of TiO_2. XRD patterns of Bi_4NbO_8Cl synthesized at 800 ℃ (D) and TiO_2 (E). (F) UV–vis diffuse reflectance spectrum of Bi_4NbO_8Cl synthesized at 800 ℃. (G) Schematic illustration of the mechanism for the charge separation and transfer in the Bi_4NbO_8Cl/TiO_2 system under UV light illumination.

84–0843). And X-ray photoelectron spectroscopy (XPS) analysis of Bi_4NbO_8Cl was shown in the Supporting Information (Fig. S1). As is well known, TiO_2 exists in two common stable crystal forms: rutile and anatase. The band gap of the rutile form (E_g: 3.0 eV) is slightly smaller than that of the anatase form (E_g: 3.2 eV). The rutile crystal form is tetragonal with a titanium atom at the center of the lattice surrounded by six oxygen atoms arranged at the vertices of a regular octahedron. The specific structure can effectively promote electron-hole separation and thus produce a higher photocurrent signal. The purchased TiO_2 often contains a mixture of anatase and rutile forms. Therefore, TiO_2 need to be calcined in a muffle furnace at 450 ℃ for 2 h to transform all the crystal forms into the rutile structure. After high-temperature calcination, the XRD pattern (Fig. 1E) manifested a typical characteristic peak (1 1 0) of rutile TiO_2 crystal plane, confirming the formation of rutile TiO_2. The peaks (1 0 1), (1 1 1), (210), (211), (220) and (301) corresponded to the planes of TiO_2 referring to the standard TiO_2 (JCPDS card 21–1276). The absorption range of the prepared rutile product was broader than that of other crystal forms, which is beneficial to its application in photoelectric determination field.

The ultraviolet–visible (UV–vis) diffuse reflection spectrum of Bi_4NbO_8Cl synthesized at 800 ℃ showed a broad absorption ranging from 200 to 500 nm and the absorption edge at 502 nm (Fig. 1F). The band gap energy (E_g) of Bi_4NbO_8Cl was calculated by the equation, $\alpha h\nu = A(h\nu - E_g)^{n/2}$, where α, h, ν, and A are the absorption coefficient, Planck constant, light frequency and a constant, respectively. Because Bi_4NbO_8Cl is an indirect bandgap semiconductor, the E_g of Bi_4NbO_8Cl was 2.36 eV taking $n = 1/2$ [31]. The possible mechanism of the prepared Bi_4NbO_8Cl/TiO_2 heterostructure was shown in Fig. 1G. Under xenon lamp irradiation, Bi_4NbO_8Cl can be excited and generates photoelectrons. Photoelectrons transfer from the upper conduction band (CB) of Bi_4NbO_8Cl to the lower CB of TiO_2, and further transfer to the external circuit. While the photogenerated holes transfer from the lower valence band (VB) of TiO_2 to the higher VB of Bi_4NbO_8Cl, and eventually be quenched by electron donors (such as AA) in electrolyte solution. Hence, the spatial modulation of electrons and holes evidently achieves the efficient separation, greatly suppressing the recombination rate and thus significantly enhancing the photocurrent intensity.

3.3. Analysis of the target-binding capability

The binding interaction among the target, auxiliary and capture probes was assessed via isothermal titration calorimetry (ITC) measurements. In Table S2, the association constant (K_a) among target/auxiliary/capture probes was *ca.* $5.0 \times 10^7\ M^{-1}$ (Fig. 2A). Nevertheless, the binding affinity between auxiliary and capture probes greatly decreased (Fig. 2B, $K_a = 6.1 \times 10^3\ M^{-1}$). Therefore, the hybridization of capture/auxiliary/target sequences possessed high binding affinity, suggesting that the Y-shaped junction structure could be stably formed,

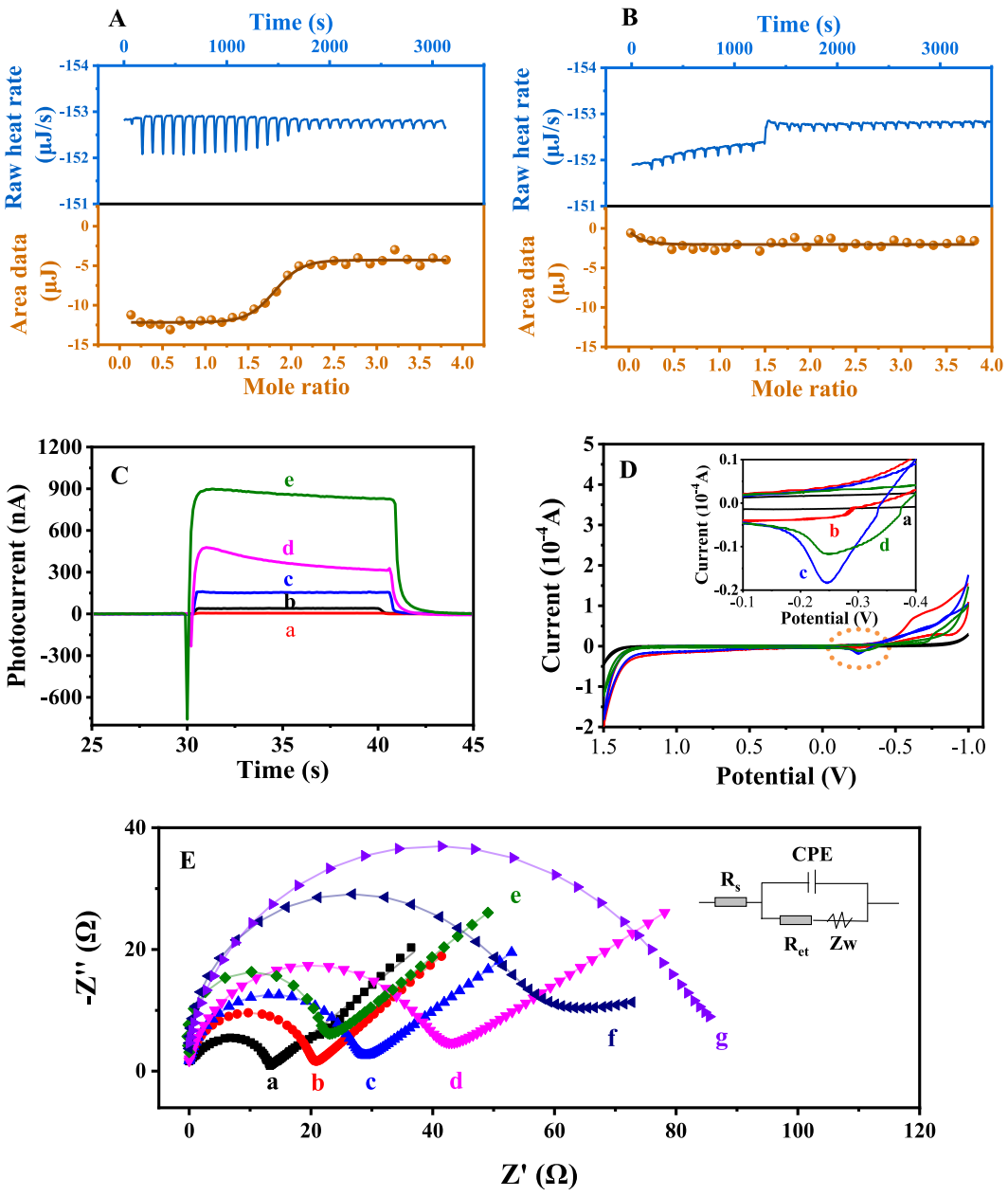

Fig. 2. (A) ITC measurements of capture probes binding to auxiliary/target sequences. (B) ITC measurements of capture probes binding to auxiliary probes. (C) Photocurrents generated from different modified ITO electrodes in PBS containing 100 mM AAP. (a) TiO_2/ITO; (b) Bi_4NbO_8Cl/ITO; (c) Bi_4NbO_8Cl/TiO_2/ITO; (d) CP/AuNPs/Bi_4NbO_8Cl/TiO_2/ITO; (e) ALP-AuNPs-AP-RNA-CP/AuNPs/Bi_4NbO_8Cl/TiO_2/ITO. (D) CV curves of the modified electrodes in 20 mM PBS solution. (a) Bare ITO; (b) TiO_2/ITO; (c) Bi_4NbO_8Cl/ITO; (d) Bi_4NbO_8Cl/TiO_2/ITO. The inset showed a close look of the yellow dotted circle. (E) EIS of different modified sensors. (a) Bare ITO; (b) TiO_2/ITO; (c) Bi_4NbO_8Cl/ITO; (d) Bi_4NbO_8Cl/TiO_2/ITO; (e) AuNPs/Bi_4NbO_8Cl/TiO_2/ITO; (f) CP/AuNPs/Bi_4NbO_8Cl/TiO_2/ITO; (g) ALP-AuNPs-AP-RNA-CP/AuNPs/Bi_4NbO_8Cl/TiO_2/ITO.

which was consistent with literature [24,25]. The significant difference in binding affinity between the individual probes and the complete probes-target complex further highlights the selectivity of the biosensor for the target miRNA.

3.4. Characterization of the modified electrodes

The stepwise assembly process of the PEC biosensor was investigated via *i-t* method, cyclic voltammetry (CV) and electrochemical impedance spectroscopy (EIS). Foremost, the photocurrent response was compared among different electrodes in PBS containing 100 mM AAP (Fig. 2C). The individual modifications of TiO_2 or Bi_4NbO_8Cl on the electrode surface generated a certain photocurrent response due to the intrinsic photoactivity of these materials (curve a and curve b). When TiO_2 and Bi_4NbO_8Cl co-immobilized, the signal value obviously enhanced, which was 30.6 times of TiO_2/ITO and 3.9 times of Bi_4NbO_8Cl/ITO, demonstrating the formation of a heterojunction structure (curve c). The synthesis temperature and time were optimized in Fig. S2. The preparation and characterization of AuNPs were exhibited in Fig. S3. With introduction of AuNPs and CP, the photocurrent signal increased (curve d). After incubation with miRNA-222 and ALP-AuNPs-AP, the Y-shaped junction structures were formed on the electrode surface, resulting in the AA production through catalyzed hydrolysis of AAP by ALP. AA could act as an electron donor to capture the holes, thereby inhibiting the electron-hole recombination and greatly enhancing the photocurrent signal (curve e). These results verified the successful construction of PEC

biosensor.

Furthermore, CV characterization of the prepared PEC biosensor was carried out in 20 mM PBS (pH = 7.4). In Fig. 2D, there was no obvious peak appeared at the bare ITO (curve a) and ITO electrode coated with 2 mg/mL TiO_2 suspension (curve b). Remarkably, an oxidation peak at *ca.* −0.25 V was observed in CV curve after the modification with 2 mg/mL Bi_4NbO_8Cl (curve c), attributing to the surface oxidation of the perovskite from Bi (III) to a higher oxidation state. Upon the formation of the Bi_4NbO_8Cl/TiO_2 heterojunction, the oxidation peak signal was slightly weakened (inset of Fig. 2D, curve d), illustrating the successful construction of the heterojunction for the designed PEC biosensor, which was further validated by the SEM image (Fig. S4). To further ascertain the interface connectivity during the layer-by-layer modification, the EIS experiment was executed in 10 mM $K_3[Fe(CN)_6]/K_4[Fe(CN)_6]$ solution with 0.1 M KCl. As shown in Fig. 2E, the bare ITO electrode (curve a) displayed a low electron transfer resistance (R_{et}, 13.57 Ω), suggesting its high electron transfer efficiency. After TiO_2 and Bi_4NbO_8Cl were respectively attached to the ITO electrode, the R_{et} values gradually increased due to the weak conductivity of these semiconductors (curve b and curve c, 18.08 and 25.90 Ω). As expected, the R_{et} value of Bi_4NbO_8Cl/TiO_2/ITO further elevated (curve d, 39.97 Ω). The growth of AuNPs on the electrode led to a slight decrease in the R_{et} value, owing to the electrical conductivity of AuNPs (curve e, 19.56 Ω). With immobilization of CP (curve f, 51,41 Ω) or Y-shaped junction structure (ALP-AuNPs-AP-RNA-CP, curve g, 73.36 Ω) on the electrode surface, the R_{et} value dramatically enhanced, because of the incremental steric hindrance among nucleic acids. In view of the above measurement results, the successful integration of the designed PEC sensor was confirmed.

3.5. Optimization of determination condition

For the sensitive analysis of the target miRNA-222, the hybridization temperature and hybridization time were optimized and depicted in Supporting Information. In short, a hybridization temperature of 37 ℃ and a hybridization time of 50 min were determined to be optimal (Fig. S5).

3.6. Analytical performance

Under the optimal experimental conditions, the developed PEC biosensor was applied for the determination of miRNA-222. As the increment of miRNA-222 concentration, the photocurrent signals continuously increased (Fig. 3A), because the gradual increment of ALP-AuNPs-AP was introduced by the Y-shaped configuration on the electrode surface, which catalyzed the hydrolysis of AAP to generate more AA, thereby enhancing the photocurrent response. As displayed in Fig. 3B, the photocurrent responses linearly increased with incremental logarithm of miRNA-222 concentration in the range from 1.0 pM to 0.1 μM. The linear equation was I (nA) = 76.14 lg$C$ (μM) + 938.50 with a linear coefficient of 0.998. The limit of detection (LOD) was calculated as low as 0.15 pM (S/N = 3, concentration at which the detected signal value is 3 times the standard deviation of the blank), exhibiting the great sensitivity to target miRNA-222. The proposed PEC biosensor possessed wide linear range, high sensitivity and low detection limit toward target miRNA-222 determination, compared with other counterparts (Table 1). Furthermore, selectivity, a critical parameter in the nucleic acid bioanalysis application, was assessed by examining the effect of various coexisting RNA sequences, including miRNA-155, miRNA-21, and miRNA-126 at the same concentration (100 nM) on the photocurrent changes. As illustrated in Fig. 3C, ΔI was the photocurrent signal generated by different miRNAs after the background signal of the CP/AuNPs/Bi_4NbO_8Cl/TiO_2/ITO electrode was deducted. Compared to experimental group (100 nM miRNA-222 group, b group), the photocurrent responses generated by other RNA sequences (c, d and e groups) were obviously

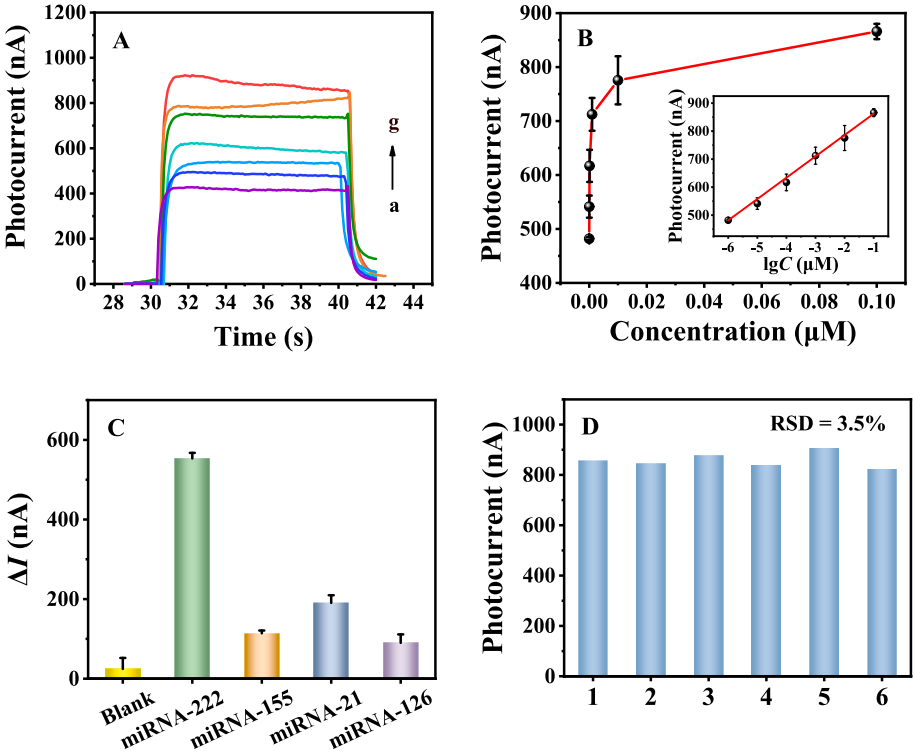

Fig. 3. (A) Photocurrent response of the Y-shape-structured PEC biosensors with various miRNA-222 concentrations (curve a to g: 0, 10^{-6}, 10^{-5}, 10^{-4}, 10^{-3}, 10^{-2}, 10^{-1} μM miRNA-222). The data were mean ± standard deviation values of three independent experiments (n = 3). (B) Point plots between photocurrent signals and miRNA-222 concentrations. Inset: Linear relationship between photocurrent signal and the logarithm of the miRNA-222 concentrations (lg$C$). (C) Selectivity of the Y-shape-structured PEC biosensors for miRNA-222 determination. The data were mean ± standard deviation values of three independent experiments (n = 3). (D) Reproducibility of the Y-shape-structured PEC biosensors for 100 nM miRNA-222 detection.

Table 1
Comparison of different methods for miRNA-222 detection.

Detection method	Strategy	Linear range	Detection limit	Reference
Colorimetry	Chromogenic reaction-free distance-based microfluidic paper-based analytical devices	1–20 pM	0.37 pM	[32]
Fluorescence	DNA-functionalized light-harvesting nanoantenna	5–200 pM	1.70 pM	[33]
Surface enhanced raman scattering	Silvered polydimethylsiloxane (PDMS)-supported porous silicon membrane	0.5–50 nM	485 pM	[34]
Electrochemistry	Magnetic bead-based bioassay	0–1 nM	7 pM	[35]
Electrochemistry	DNA-RNA complementation on silicon wafer	1 fM–10 pM	1 fM	[36]
ECL	Carbon quantum dots and Y-shaped junction structure equipped with locked nucleic acids	0.025–50 pM	1.95 fM	[24]
PEC	Dual signal amplification tactic based on Bi_4NbO_8Cl/TiO_2 heterojunction and enzyme-mediated electrocatalysis	1 pM–0.1 μM	0.15 pM	This work

smaller, revealing the developed PEC biosensor exhibited good specificity toward target sequence. The improved selectivity can be contributed to the formation of Y-shaped DNA junction structure on the electrode surface upon miRNA hybridizing across the two branches. Additionally, to evaluate the reproducibility of the sensor, six parallel measurements were carried out under identical experimental condition with 100 nM miRNA-222. The relative standard deviation (RSD) value was 3.5 % (Fig. 3D), demonstrating the PEC biosensor possessed a favorable reproducibility.

3.7. Real sample analysis and recovery study

To assess the feasibility and potential application of the PEC biosensor in real sample determination, the biosensor was challenged with different concentrations of miRNA-222 spiked into 1000-fold diluted normal human serum. Each determination was conducted three times. In Table 2, the recoveries all lied in the range of 97.8 % – 98.7 % and the RSD values were 2.9 %, 3.0 % and 3.7 %, respectively. The above results illustrated the developed PEC biosensor's great resistance to interference and feasibility in real sample analysis.

Table 2
Recovery study for miRNA-222 in human serum (n = 3).

Sample	Spiked (pM)	Recovery (%)			Mean recovery (%)	RSD (%)
1	10	94.8	101	97.8	97.8	2.9
2	100	98.6	102	95.7	98.7	3.0
3	1000	93.8	98.4	101	97.8	3.7

4. Conclusions

In summary, a sensitive and selective Y-shape-structured PEC biosensor coupled with dual signal enhancement strategy, comprising the employment of Bi_4NbO_8Cl/TiO_2 heterostructure and electron donor-AA generated by ALP catalysis, was developed for PTC-related miRNA-222 determination. It is noteworthy that the utilization of TiO_2 could not only enhance the photocurrent intensity beyond that of Bi_4NbO_8Cl alone due to efficient separation of charge carriers, but also lay a foundation for probe hybridization. Meanwhile, upon miRNA-222 introduction, the formation of Y-shaped hybridization configuration demonstrated remarkable molecular rigidity and excellent resistance to interference. Moreover, the ALP connected to the biosensor surface catalyzed AAP to generate AA, which evidently enhanced the photocurrent signals. Comprehensively, the proposed PEC biosensor stands out for its high sensitivity and low detection limit toward miRNA-222 determination. And the high anti-interference properties, excellent selectivity and reproducibility of the proposed PEC biosensor endowed its application in the real sample analysis. It is believed that the developed Y-shape-structured PEC biosensor, empowered by dual signal amplification tactic can ignite new avenues for developing advanced schemes toward bioanalysis.

Admittedly, there are still some limitations existed in the developed PEC biosensing method. On the one hand, the binary heterostructures have relatively simple carrier transport pathways with limited channels for electron and hole transport. Ternary heterostructures can optimize carrier transport pathways by introducing a third material, forming a more complex transport network and thereby improving carrier mobility. On the other hand, the developed single-signal mode PEC biosensor is highly susceptible to interference from environmental factors (such as changes in light intensity and temperature) as well as background signals, which can lead to decreased accuracy, sensitivity and interference resistance. In contrast, dual-signal mode ratiometric PEC biosensor can effectively achieve self-calibration, lower detection limit and mitigate interference. Hence, the PEC biosensor equipped with ternary heterostructures and dual-signal mode is the direction of our future efforts.

CRediT authorship contribution statement

Yu Zhong: Writing – original draft, Investigation, Formal analysis. **Zhi-Wei Xu:** Investigation, Formal analysis. **Zhang-Jian Cheng:** Investigation. **Ai-Lin Liu:** Writing – review & editing, Resources, Project administration. **Yun Lei:** Writing – review & editing, Supervision, Resources, Project administration.

Declaration of competing interest

The authors declare that they have no known competing financial interests or personal relationships that could have appeared to influence the work reported in this paper.

Acknowledgements

The authors gratefully acknowledge the financial support of the National Natural Science Foundation of China (82373838), the Natural Science Foundation of Fujian Province of China (2023J01551) and Joint Funds for the Innovation of Science and Technology, Fujian Province (2024Y9111). The authors would like to thank Yan Hu from the Public Technology Service Center (Fujian Medical University, Fuzhou, China) for technical assistance.

Appendix A. Supplementary data

Supplementary data to this article can be found online at https://doi.org/10.1016/j.microc.2025.113954.

Data availability

No data was used for the research described in the article.

References

[1] J.K. Cheong, Y.C. Tang, L. Zhou, H. Cheng, H.P. Too, Advances in quantifying circulatory microRNA for early disease detection, Curr. Opin. Biotech. 74 (2022) 256–262.

[2] X. Yu, Y. Zhang, F. Luo, Q. Zhou, L. Zhu, The role of microRNAs in the gastric cancer tumor microenvironment, Mol. Cancer 23 (2024) 170.
[3] S. Lin, R.I. Gregory, MicroRNA biogenesis pathways in cancer, Nat. Rev. Cancer 15 (2015) 321–333.
[4] D. Mukhopadhyay, P. Cocco, S. Orrù, R. Cherchi, S.D. Matteis, The role of MicroRNAs as early biomarkers of asbestos-related lung cancer: A systematic review and meta-analysis, Pulmonology S2531–0437 (2024) 00015.
[5] Y. Zhao, J. Xiang, H. Cheng, X. Liu, F. Li, Flexible photoelectrochemical biosensor for ultrasensitive microRNA detection based on concatenated multiplex signal amplification, Biosens. Bioelectron. 194 (2021) 113581.
[6] T. Jet, G. Gines, Y. Rondelez, V. Taly, Advances in multiplexed techniques for the detection and quantification of microRNAs, Chem. Soc. Rev. 50 (2021) 4141–4161.
[7] X. Meng, X. Pang, J. Yang, X. Zhang, H. Dong, Recent advances in electrochemiluminescence biosensors for MicroRNA detection, Small 20 (2024) e2307701.
[8] Y. Li, X. Li, Y. Meng, X. Hun, Photoelectrochemical platform for MicroRNA let-7a detection based on graphdiyne loaded with AuNPs modified electrode coupled with alkaline phosphatase, Biosens. Bioelectron. 130 (2019) 269–275.
[9] E. Ma, K. Wang, Y. Gou, W. Luo, H. Wang, Dual-responsive MnO_2-loaded carbonaceous nanobottle motors fabricated by interfacial superassembly for on-the-fly microRNA sensing, Small (2024) e2404703.
[10] Z.L. Ma, J.J. Chen, X.F. Sun, Y. Xie, H. Luo, K.J. Huang, X. Tan, Y.L. Tang, Target-triggered multiple-polarity-switchable multiplexed photoelectrochemical platform, Anal. Chem. 96 (2024) 14918–14925.
[11] J. Li, C. Chen, F. Luo, C. Lin, Z. Lin, J. Wang, B. Qiu, Dual-signal mode ratiometric photoelectrochemical sensor based on G-quadruplex hole transport for rapid and sensitive detection of miRNA-210, Anal. Chem. 95 (2023) 17670–17678.
[12] T.K. Wang, D.G. Jiang, Y.T. Shi, Z.H. Wang, G.J. Liu, S.X. Lin, H. Zhou, Q. Wang, ZnS/MXene/CdS heterostructure modified electrode for ultrasensitive miRNA-21 assay with signal amplified photoelectrochemical strategy, Sensor. Actuat. B-Chem. 419 (2024) 136435.
[13] W. Wang, M. Xu, X. Xu, W. Zhou, Z. Shao, Perovskite oxide based electrodes for high-performance photoelectrochemical water splitting, Angew. Chem. Int. Edit. 59 (2020) 136–152.
[14] K. Bienkowski, R. Solarska, L. Trinh, J. Widera-Kalinowska, B. Al-Anesi, M. Liu, G. K. Grandhi, P. Vivo, B. Oral, B. Yılmaz, R. Yıldırım, Halide perovskites for photoelectrochemical water splitting and CO_2 reduction: Challenges and opportunities, ACS Catal. 14 (2024) 6603–6622.
[15] J.F. Ackerman, The structures of Bi_3PbWO_8Cl and Bi_4NbO_8Cl and the evolution of the bipox structure series, J. Solid State Chem. 62 (1986) 92–104.
[16] H. Fujito, H. Kunioku, D, Kato, H, Suzuki, M. Higashi, H. Kageyama, R. Abe, Layered perovskite oxychloride Bi_4NbO_8Cl: A stable visible light responsive photocatalyst for water splitting, J. Am. Chem. Soc. 138 (2016) 2082-2085.
[17] E. Shi, Y. Gao, B.P. Finkenauer, A.H. Coffey, L. Dou, Two-dimensional halide perovskite nanomaterials and heterostructures, Chem. Soc. Rev. 47 (2018) 6046–6072.
[18] S. Bera, N. Pradhan, Perovskite nanocrystal heterostructures: Synthesis, optical properties, and applications, ACS Energy Lett. 5 (2020) 2858–2872.
[19] L. Deng, F. Ma, M. Yang, X. Li, X. Chen, A halide perovskite/lead sulfide heterostructure with enhanced photoelectrochemical performance for the sensing of alkaline phosphatase (ALP), Chem. Commun. 59 (2023) 1361–1364.
[20] Y.F. Ruan, N. Zhang, Y.C. Zhu, W.W. Zhao, J.J. Xu, H.Y. Chen, Photoelectrochemical bioanalysis platform of gold nanoparticles equipped perovskite Bi_4NbO_8Cl, Anal. Chem. 89 (2017) 7869–7875.
[21] S. Palmas, L. Mais, M. Mascia, A. Vacca, Trend in using TiO_2 nanotubes as photoelectrodes in PEC processes for wastewater treatment, Curr. Opin. Electroche. 28 (2021) 100699.
[22] H. Cheng, Y. Wang, Y. Zhao, H. Hou, G. Zhang, J. Bi, S. Yan, H. Hao, Hybrid chain reaction-based and $Au/Bi_4NbO_8Cl/In_2S_3$ layer-by-layer assembled dual-mode photoelectrochemical-electrochemical aptasensor for the detection of Salmonella enteritidis, Talanta 281 (2025) 126815.
[23] C. Gao, J. Xue, L. Zhang, K. Cui, H. Li, J. Yu, Paper-based origami photoelectrochemical sensing platform with TiO_2/Bi_4NbO_8Cl/Co-Pi cascade structure enabling of bidirectional modulation of charge carrier separation, Anal. Chem. 90 (2018) 14116–14120.
[24] Y. Zhong, L.X. Huang, M.T. Lin, Z.Y. Zhang, A.L. Liu, Y. Lei, A Y-shape-structured electrochemiluminescence biosensor based on carbon quantum dots and locked nucleic acid probe for microRNA determination with single-base resolution, Biosens. Bioelectron. 238 (2023) 115583.
[25] C. Li, D. Wu, X. Hu, Y. Xiang, Y. Shu, G. Li, One-step modification of electrode surface for ultrasensitive and highly selective detection of nucleic acids with practical applications, Anal. Chem. 88 (2016) 7583–7590.
[26] H. Zhang, X. Li, F. He, M. Zhao, L. Ling, Turn-off colorimetric sensor for sequence-specific recognition of single-stranded DNA based upon Y-shaped DNA structure, Sci. Rep-UK 8 (2018) 12021.
[27] L. Guo, Y. Xu, A.R. Ferhan, G. Chen, D.H. Kim, Oriented gold nanoparticle aggregation for colorimetric sensors with surprisingly high analytical figures of merit, J. Am. Chem. Soc. 135 (2013) 12338–12345.
[28] B. Liu, Y. Ge, Y. Lu, Y. Huang, X. Zhang, X. Yuan, An NIR light-responsive "on-off-on" photoelectrochemical aptasensor for carcinoembryonic antigen assay based on Y-shaped DNA, Biosens. Bioelectron. 229 (2023) 115241.
[29] Y.T. Chen, N. Kitabayashi, X.K. Zhou, T.J. Fahey III, T. Scognamiglio, MicroRNA analysis as a potential diagnostic tool for papillary thyroid carcinoma, Modern Pathol. 21 (2008) 1139–1146.
[30] A. Majumdar, U. Ghosh, A. Pal, Novel 2D/2D g-C_3N_4/Bi_4NbO_8Cl nano-composite for enhanced photocatalytic degradation of oxytetracycline under visible LED light irradiation, J. Colloid Interf. Sci. 584 (2021) 320–331.
[31] J. Ding, Y. Zhou, Q. Wang, S. Ai, Photoelectrochemical biosensor for DNA hydroxymethylation detection based on the enhanced photoactivity of in-situ synthesized $Bi_4NbO_8Cl@Bi_2S_3$ heterojunction, Biosens. Bioelectron. 194 (2021) 113580.
[32] L. Zhang, J. Chen, H. Yang, Z. Yu, Y. Xu, S.Y. Liu, Z. Dai, X. Zou, A chromogenic reaction-free distance-based paper device for facile detection of microRNA via viscosity amplification and surface hydrophobicity modulation, Sensor. Actuat. B-Chem. 359 (2022) 131570.
[33] S. Egloff, N. Melnychuk, A. Reisch, S. Martin, A.S. Klymchenko, Enzyme-free amplified detection of cellular microRNA by light-harvesting fluorescent nanoparticle probes, Biosens. Bioelectron. 179 (2021) 113084.
[34] A. Chiadò, C. Novara, A. Lamberti, F. Geobaldo, F. Giorgis, P. Rivolo, Immobilization of oligonucleotides on metal-dielectric nanostructures for miRNA detection, Anal. Chem. 88 (2016) 9554–9563.
[35] F. Bettazzi, E. Hamid-Asl, C.L. Esposito, C. Quintavalle, N. Formisano, S. Laschi, S. Catuogno, M. Iaboni, G. Marrazza, M. Mascini, L. Cerchia, V.D. Franciscis, G. Condorelli, I. Palchetti, Electrochemical detection of miRNA-222 by use of a magnetic bead-based bioassay, Anal. Bioanal. Chem. 405 (2013) 1025–1034.
[36] S.C. Gopinath, S. Xuan, DNA-RNA complementation on silicon wafer for thyroid cancer determination, Appl. Bioc. 68 (2021) 554–559.